Geophysical Research Letters

RESEARCH LETTER
10.1029/2020GL087221

A Long-Lived Sharp Disruption on the Lower Clouds of Venus

J. Peralta[1], T. Navarro[2,3,4], C. W. Vun[1], A. Sánchez-Lavega[5], K. McGouldrick[6], T. Horinouchi[7], T. Imamura[8], R. Hueso[5], J. P. Boyd[9], G. Schubert[2], T. Kouyama[10], T. Satoh[1], N. Iwagami[11], E. F. Young[12], M. A. Bullock[12], P. Machado[13], Y. J. Lee[14], S. S. Limaye[15], M. Nakamura[1], S. Tellmann[16], A. Wesley[17], and P. Miles[18]

[1]Institute of Space and Astronautical Science, JAXA, Sagamihara, Japan, [2]Department of Earth, Planetary, and Space Sciences, University of California, Los Angeles, Los Angeles, CA, USA, [3]McGill Space Institute, McGill University, Montréal, Quebec, Canada, [4]Department of Earth and Planetary Sciences, McGill University, Montréal, Quebec, Canada, [5](5) Escuela de Ingeniería de Bilbao, UPV/EHU, Bilbao, Spain, [6]Laboratory for Atmospheric and Space Physics, University of Colorado Boulder, Boulder, CO, USA, [7]Faculty of Environmental Earth Science, Hokkaido University, Hokkaido, Japan, [8]Graduate School of Frontier Sciences, The University of Tokyo, Tokyo, Japan, [9]CLaSP Department, University of Michigan College of Engineering, Ann Arbor, MI, USA, [10]Artificial Intelligence Research Center, National Institute of Advanced Industrial Science and Technology, Tokyo, Japan, [11]Tokyo, Japan, [12]Southwest Research Institute, Boulder, CO, USA, [13]Institute of Astrophysics and Space Sciences, Lisbon, Portugal, [14]Abteilung Planetenforschung, Rheinisches Institut für Umweltforschung, Universität zu Köln, Köln,Germany, [15]Space Science and Engineering Center, University of Wisconsin, Madison, WI, USA, [16]Abteilung Planetenforschung, Rheinisches Institut für Umweltforschung, Universität zu Köln, Cologne, Germany, [17]Astronomical Society of Australia, Murrumbateman, New South Wales, Australia, [18]Gemeye Observatory, Rubyvale, Queensland, Australia

Abstract Planetary-scale waves are thought to play a role in powering the yet unexplained atmospheric superrotation of Venus. Puzzlingly, while Kelvin, Rossby, and stationary waves manifest at the upper clouds (65–70 km), no planetary-scale waves or stationary patterns have been reported in the intervening level of the lower clouds (48–55 km), although the latter are probably Lee waves. Using observations by the Akatsuki orbiter and ground-based telescopes, we show that the lower clouds follow a regular cycle punctuated between 30°N and 40°S by a sharp discontinuity or disruption with potential implications to Venus's general circulation and thermal structure. This disruption exhibits a westward rotation period of ~4.9 days faster than winds at this level (~6-day period), alters clouds' properties and aerosols, and remains coherent during weeks. Past observations reveal its recurrent nature since at least 1983, and numerical simulations show that a nonlinear Kelvin wave reproduces many of its properties.

Plain Language Summary One of the biggest mysteries of Venus is its atmospheric superrotation that allows the atmosphere to rotate 60 times faster than the solid planet. Atmospheric waves are among one of the possible mechanisms thought to feed this superrotation by pushing energy to different locations of the atmosphere. In fact, the upper clouds of Venus located at 65–70 km exhibit varied giant waves, like the so-called Y feature or the more recently discovered bow-shaped wave that keeps "stationary" over Aphrodite mountains. In contrast, these planetary-scale waves are missing at the deeper lower clouds (48–55 km). This is especially puzzling in the case of the stationary waves since the lower clouds are located between the upper clouds and the surface, where they are thought to be generated. Thanks to the high-quality observations of Venus from JAXA's space mission Akatsuki and NASA's IRTF telescope, we discovered at the lower clouds an intriguing sharp discontinuity that propagates to the west faster than the winds while altering the clouds' properties and suffering little distortions during weeks. A reanalysis of past observations revealed that this is a recurrent phenomenon that has gone unnoticed since at least the year 1983. Numerical simulations evidence that an atmospheric wave generated below the clouds and probably pumping energy to the upper clouds can explain many of its properties.

Key Points:
- Discovery of an equatorial cloud discontinuity at the middle and lower clouds of Venus, where no planetary wave had been found before
- This disruption propagates to the West faster than the winds, keeps coherent for weeks, and alters clouds' properties and aerosols
- Past observations confirm its existence since 1983; numerical simulations suggest a physical origin as a nonlinear Kelvin wave

Supporting Information:
- Supporting Information S1

Correspondence to:
J. Peralta,
javier.peralta@ac.jaxa.jp

Citation:
Peralta, J., Navarro, T., Vun, C. W., Sánchez-Lavega, A., McGouldrick, K., Horinouchi, T., et al. (2020). A long-lived sharp disruption on the lower clouds of Venus. *Geophysical Research Letters*, *47*, e2020GL087221. https://doi.org/10.1029/2020GL087221

Received 23 JAN 2020
Accepted 1 MAY 2020

1. Introduction

The atmosphere of Venus is dominated by superrotating winds that at the cloud layers (~48–70 km) (Titov et al., 2018) exhibit speeds 60 times faster than the planet (Sánchez-Lavega et al., 2017). The clouds of Venus

are mostly composed of H_2SO_4-H_2O droplets and are stratified into three layers (Titov et al., 2018). In the upper clouds (56.5–70 km above the surface), absorbers of known and unknown composition are responsible for the dark markings observed in ultraviolet images and for most of the absorption of the solar energy not reflected by the clouds (Titov et al., 2018). The middle and lower clouds (hereafter, simply named *deeper clouds*) are within 47.5–56.5 km and importantly contribute to the greenhouse effect and the radiative energy balance. These clouds exhibit variable cloud optical thickness (McGouldrick et al., 2012; Peralta et al., 2019; Titov et al., 2018) in a region where the lapse rate is close to adiabatic and convection dominates vertical transport, as shown by observations (Ando et al., 2020; Hinson & Jenkins, 1995; Tellmann et al., 2009; Yakovlev et al., 1991) and modeling (Imamura et al., 2014; Lefèvre et al., 2018). The middle clouds (50.5–56.5 km) are observed on the dayside at visible and near-infrared (900–1,000 nm) wavelengths (Peralta et al., 2019; Titov et al., 2018), while the lower clouds (47.5–50.5 km) are observed on the nightside using spectral windows at 1.74, 2.26, and 2.32 μm (Limaye et al., 2018; McGouldrick et al., 2012; Titov et al., 2018). Clouds' morphology and motions are different at each of these layers (Horinouchi et al., 2017; Limaye et al., 2018; Peralta et al., 2019; Sánchez-Lavega et al., 2017; Titov et al., 2018).

It has long been proposed that planetary-scale waves could play a role in powering the superrotation (Sánchez-Lavega et al., 2017). Some of them manifest visually at the upper clouds (65–70 km), like the Y feature (Peralta et al., 2015) and the stationary bow-shaped wave (Fukuhara et al., 2017). Some others manifest in the wind field like thermal tides (Kouyama et al., 2019), Kelvin and Rossby waves (Imai et al., 2019), and stationary features (Peralta et al., 2017). However, no planetary-scale waves or stationary patterns have been reported in the intervening level of the lower clouds (Peralta et al., 2008, 2017; Peralta, Sánchez-Lavega et al., 2019; Peralta, Iwagami et al., 2019) (48–55 km), even though stationary waves are probably generated at the surface (Navarro et al., 2018).

2. Methods

The nightside lower clouds of Venus were studied using 1,519 images acquired at 1.735, 2.26, and 2.32 μm during April–November 2016 by the IR2 camera (Satoh et al., 2017) onboard the Akatsuki orbiter (Nakamura et al., 2016), giving preference to 2.26-μm images (238 useful images), which were less affected by light contamination from the saturated dayside (Satoh et al., 2017). The periods January–February 2017, November–December 2018, and January 2019 were studied with 78 K_{cont} (2.32-μm) images from the instruments SpeX and iSHELL (Rayner et al., 2003, 2012) at NASA's Infrared Telescope Facility (IRTF). We also reanalyzed 376 images from the Visible and Infrared Thermal Imaging Spectrometer (VIRTIS) covering April 2006 to October 2008 during the Venus Express (VEx) mission (Drossart et al., 2007). The dayside middle clouds were inspected from December 2015 to December 2016 using 984 Akatsuki/IR1 900-nm images (Iwagami et al., 2018), although October 2016 was covered with 29 1-μm images from a 0.5-m ground-based telescope since the phase angle from Akatsuki was large. The spatial resolution of Akatsuki images ranges 74–0.2 km/pixel depending on the distance between the spacecraft and the planet (Nakamura et al., 2016), while for ground-based observations it varies from 29–65 km (IRTF) to 400 km (0.5-m telescope) (Sánchez-Lavega et al., 2016). A summary of the imagery data set is shown in Table S1 in the supporting information.

2.1. Image Processing

Akatsuki IR1 and IR2 cameras have CSD/CCD and PtSi-CSD/CCD detectors, respectively, with dimensions 1,024 × 1,024, and their images present some specific problems (Iwagami et al., 2018; Satoh et al., 2017). IR2 images sensing Venus's nightside at 1.74, 2.26, and 2.32 μm in the calibration version of this work (v20180201) present a problem of light contamination with halation rings and a cross pattern that extends horizontally and vertically around the saturated dayside of the planet, spreading with multiple reflections along the PtSi detector (Satoh et al., 2017). IR2 images taken with the 2.26-μm filter were chosen for the characterization of clouds' morphology and motions, since the contamination is sufficiently reduced in them. We reduced the light contamination with an image processing procedure consisting on an adjustment of the brightness/contrast, followed by convolution with unsharp-mask image filter, and finally adaptive histogram equalization (Peralta et al., 2018, 2019). This procedure is not totally efficient, and the effect of light contamination is yet apparent in some of the figures in this work (Figures 1). The images of the nightside acquired with the guide camera of IRTF/SpeX (Rayner et al., 2003) and a K_{cont} filter were subtracted with sky images and flat-fielded corrected, though they lacked absolute calibration. Light contamination from the saturated dayside was efficiently reduced by subtracting these images with others acquired with a Bγ

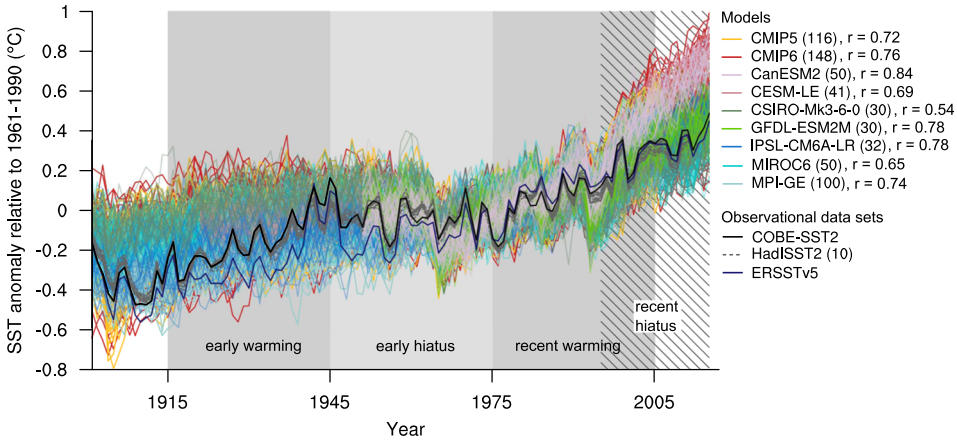

Figure 1. The cycle of the deeper clouds of Venus. Time composites of the deeper clouds displayed with overlapped equirectangular projections (60°N to 60°S and 0.5° per pixel) placed from left to right with increasing dates: (a) 18–22 August 2016 and 25–27 (IR2-2.26 μm), (b) 3–4 May 2016 (IR1-900 nm), (c) 10–17 October 2016 (IR2-2.26 μm), and (d) 1–6 December 2018 (SpeX-2.3 μm). Panel (e) exhibits the evolution of a case of disruption in 27 November and 2 and 6 December 2018 (SpeX-2.3 μm). All images display the nightside of Venus except (b).

filter (2.18 μm). The processing technique afterward was like the one applied on IR2 images, skipping the adaptive histogram equalization.

IR1 900-nm dayside images suffered from the added effect of smear noise, a brightness mismatch among the four quadrants of the camera sensor and a very small signal-to-noise (S/N) ratio (Iwagami et al., 2018). Except for the latter, these effects are reasonably well corrected in the calibration version v20180201. To increase the S/N of the IR1 images, we applied a photometric Minnaert correction (Peralta et al., 2019) followed by brightness/contrast enhancement, smoothing with a radius of 2–3 pixels and a later unsharp mask. This procedure successfully enhances the cloud features, especially in IR1 images with smaller-phase angle (and better S/N), although it also enhances brightness mismatch among the quadrants of the sensor (see Figures 1b, 2a, and 2c). The images from small telescopes were acquired with a 508-mm Newtonian telescope, a FLIR GS3-U3-32S4M-C camera, and a Thorlabs FELH1000 1 μm long-pass filter. These ground-based images covered 18 days from 9 to 30 October 2016, with a solar elongation of 35°, a mean diameter of about 13 arcsecs, and an 80% of illuminated fraction. As with the IR1/900-nm images, we applied a Minnaert photometric correction followed by unsharp mask (see examples in Figure S4).

2.2. Navigation of Images

Small uncertainties are known to affect the pointing of Akatsuki cameras, inhibiting high accuracy in the navigation of the Venus images (Ogohara et al., 2017). The image navigation was corrected using an ellipse fitting procedure where an automatic determination of the planetary limb pixels corrects the pointing (Horinouchi et al., 2017; Ogohara et al., 2017; Satoh et al., 2017). This automated method was used for the IR1 images but discarded in the case of IR2 and SpeX since light contamination and frequent darkening of the clouds' opacity make difficult the automatic identification of the planetary limb. For these images, we used a software tool (Peralta et al., 2018) which improves the visualization of the limb through image processing and allows to perform a visual adjustment of the position, size, and orientation of the planet's grid. In the case of the IR2 images, the orientation of the navigation grid is kept unmodified, while the position of the grid was adjusted with a precision of 1/10 of a pixel. Images from SpeX, iSHELL, and small telescope were first navigated using NASA's SPICE kernels, and both position and orientation of the grid were adjusted.

2.3. Calculation of Cloud Properties Using VEx/VIRTIS Images

Due to the problem of light contamination in the images of Akatsuki/IR2, we considered only VEx/VIRTIS images (see Table S1) to study the effect of the cloud discontinuity on the optical depth and size parameter of the nightside lower clouds (see Figures 3b and 3c). Prior to calculating the optical thickness and size parameter, we performed a correction of the limb darkening in images at 1.74 and 2.30 μm, following the formula given by Wilson et al. (2008):

$$I_{1.74\mu m} = \frac{I'_{1.74\mu m}}{0.316 + 0.685 \cdot \cos EA} \quad (1)$$

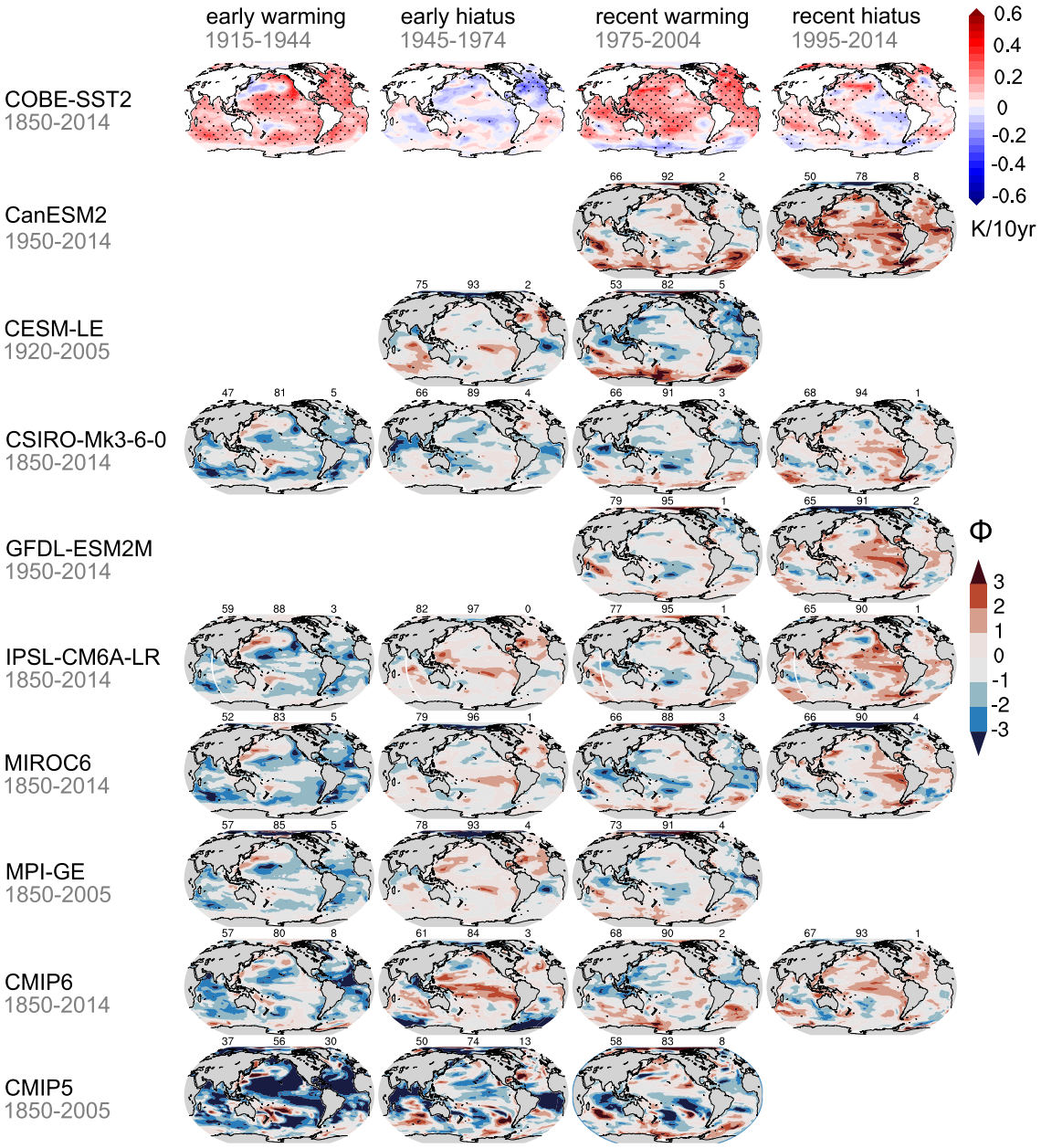

Figure 2. Morphology, vertical extension, and recurrence of Venus's disruption. (a) Morphological changes of the cloud discontinuity during 2016 on images from IR1/900-nm (dayside) and IR2/2.26-μm (nightside). Full set in Figures S2–S3; (b) example of undulations behind a discontinuity in 15 April 2016; (c) discontinuities apparent on the middle clouds (IR1) but not at the upper clouds sensed with ultraviolet (UVI) and 2.02-μm images (IR2); (d) past events of disruption (left-to-right, top-to-bottom): September 1983 (Allen & Crawford, 1984), January–February 1990 (Crisp et al., 1991), December 2005 (Bailey, 2006), September 2006 (VEx/VIRTIS), and July 2012 (Peralta et al., 2018). All images were high-pass filtered (see section 2.1). Disruptions are marked with arrows.

$$I_{2.30\mu m} = \frac{I'_{2.30\mu m}}{0.232 + 0.768 \cdot \cos EA} \quad (2)$$

where $I'_{1.74\mu m}$ and $I'_{2.30\mu m}$ are the observed radiances and EA is the emission angle.

The optical depth τ was calculated using VIRTIS images at 1.74 μm as $\tau = \log\left(I^{max}_{1.74\mu m}/I_{1.74\mu m}\right)$, where $I^{max}_{1.74\mu m}$ and $I_{1.74\mu m}$ are, respectively, the maximum value of radiance and the radiance at every pixel in the image. The size parameter m was calculated following the method of Carlson et al. (1993) using the formula adapted

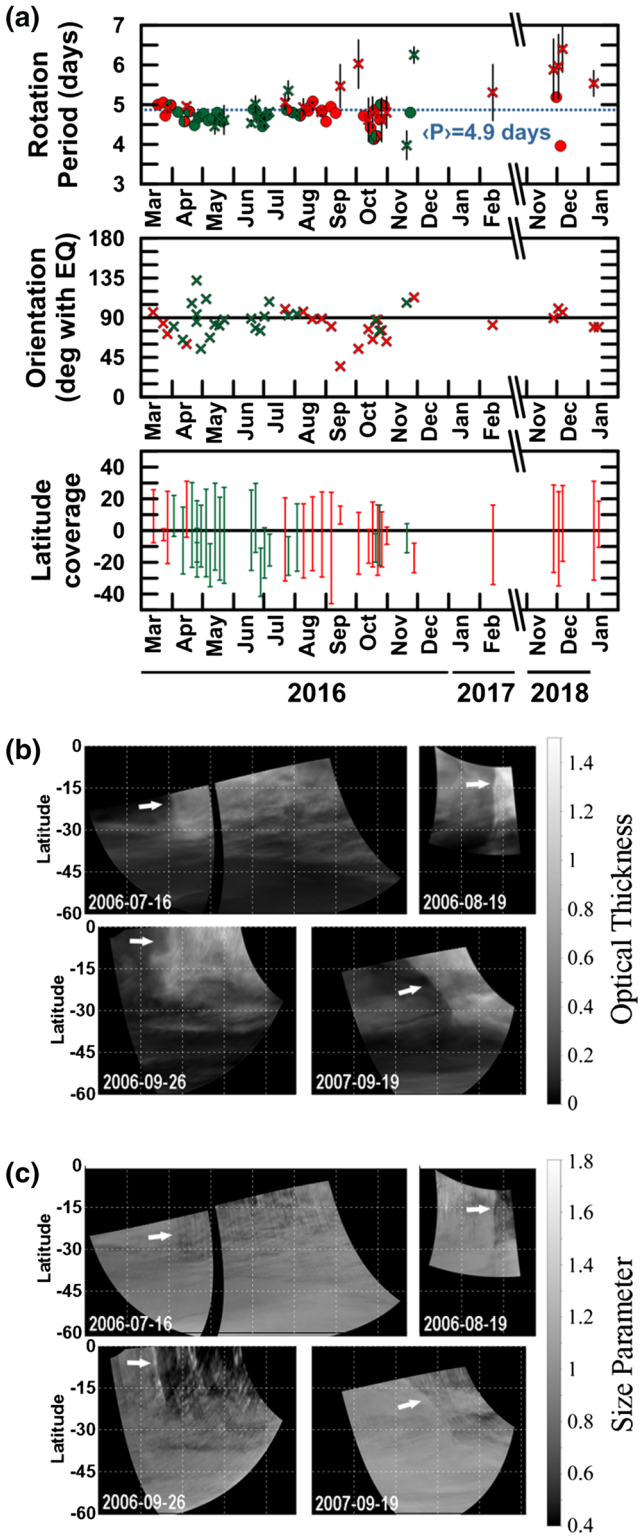

Figure 3. Properties of the cloud disruption. (a) Rotation period (mean period with blue-dotted line), orientation, and latitude coverage of the disruption along 2016–2019. The periods were measured from the position of the disruption at the equator in images separated by hours (crosses) and several days (dots). When the disruption did not intersect the equator, we considered its longitude closest to the equator. Day/nightside data are shown in green/red, respectively. (b) and (c) Effect of the disruptions over the optical thickness (1.74 μm) and size parameter (1.74 and 2.32 μm) in equirectangular projections (0–60°S, 0.2°·pix^{-1}) of VEx/VIRTIS images (see section 2.3).

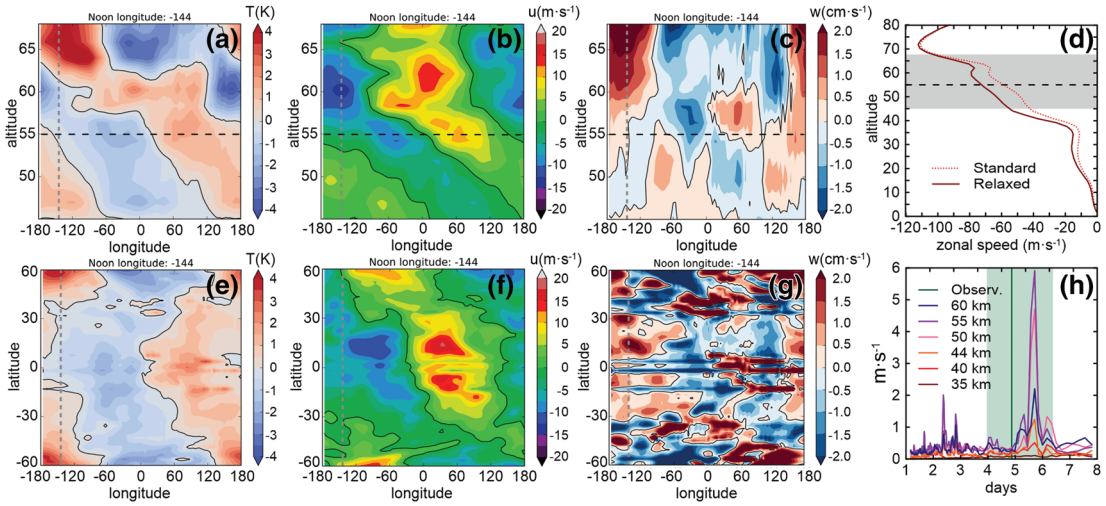

Figure 4. Kelvin wave according to a Venus GCM. Wave disturbances on temperatures and zonal and vertical speeds are shown as vertical cross sections within 45–68 km (a–c) and horizontal ones at 55 km (e–g). Panel (d) shows the standard and relaxed profiles of zonal winds (see section 2.4), with the gray-shaded area marking the altitudes in panels (a)–(c). Panel (h) displays periodograms of the zonal speeds at several altitudes, with the green line/shaded-area standing for the averaged and minimum/maximum rotation periods from observations of the disruption. Noon longitude and 55-km altitude are shown with gray and black dashed lines, respectively.

for VIRTIS by Wilson et al. (2008): $m = \left(I_{1.74\mu m}\right) / \left(I_{2.30\mu m}\right)^{0.53}$, where $I_{1.74\mu m}$ and $I_{2.30\mu m}$ are the calibrated radiances of the Venus images at 1.74 and 2.30 μm.

2.4. Simulations with the IPSL Venus GCM

The IPSL (Institut Pierre-Simon Laplace) GCM (general circulation model) is a full-physics model that includes, among other things, radiative transfer for solar and thermal radiations, a boundary layer scheme, topography, hybrid vertical coordinates, and a temperature-dependent heat capacity (Garate-Lopez & Lebonnois, 2018; Lebonnois et al., 2010). The resolution used for the longitude-latitude grid is 96 × 96, and the configuration is the same as that in Garate-Lopez and Lebonnois (2018), who arbitrarily increased solar heating rates of the poorly constrained properties of the lower haze below the cloud base in order to match observed temperatures. Superrotation is fully developed in numerical simulations with this model after 300 Venus solar days of simulation.

The GCM predicts zonal speeds of 45 m s^{-1} at the bottom of the cloud deck (48 km) (see Figure 4d), slower than the 60 m s^{-1} from in situ measurements by Pioneer Venus descent probes (Counselman et al., 1980). To correct this, we added an extra term in the dynamic core of the model to the equation of zonal momentum for latitudes equatorward of 50°:

$$\frac{du}{dt} = \ldots + \left(u_f - u\right) \cdot k(P) \tag{3}$$

with u being the zonal wind, u_f the forced zonal wind profile, and $k(P)$ a pressure-dependent coefficient:

$$k(P) = 10^{-6} \cdot \frac{1 + \tanh\left(\log\left(P/10^5\right)\right)}{2} \tag{4}$$

The forced wind zonal profile u_f is constructed from the temporally and zonally averaged zonal winds from the standard simulation of Garate-Lopez and Lebonnois (2018), increased by 30%. This relaxed simulation starts from the initial state of fully developed superrotation from the standard simulation, and it converges to increased steady averaged zonal winds in less than a Venus day.

3. Results

To study the global opacity and morphology of the deeper clouds over several revolutions of the mean flow (~5–6 day period; see Horinouchi et al., 2017; Peralta et al., 2018; Peralta et al., 2019), we constructed time composites combining equirectangular projections of the images shifted according to the zonal background

wind (see Figure 1; animations of Figures 1c and 1e can be found in Movie S1). At low latitudes, the nightside lower clouds show a variable dark band (higher opacity) (Crisp et al., 1991), while bright (lower opacity) bands dominate at midlatitudes. The lower clouds drift to the west following a ~5–6-day cycle. The equatorial band dominated by dark featureless clouds (longitude drift 40°–100° in Figure 1a or 240°–300° in Figure 1b) is observed to become narrower as midlatitude bands gradually invade lower latitudes. Simultaneously, it exhibits bright swirls and other patterns reminiscent of von Kármán vortex streets (Figure 1a) and the borders with the midlatitude bands adopt a wavy shape (wavelengths ranging 4,000–6,000 km) with mesoscale billows and vortices (Horinouchi et al., 2017; Peralta et al., 2019; Satoh et al., 2017). The cycle ends when the dark band develops brighter clouds that are abruptly interrupted by a sharp discontinuity or disruption. During August 2016 (Figure 1a), an equatorial jet was observed (Horinouchi et al., 2017) ~150°–200° west from the disruption. In October 2016 (Figure 1c), the discontinuity became weaker, the equatorial jet seemed missing, and the midlatitude bands merged at the equator forming a bright trough (Peralta et al., 2019). An examination of 85 radio occultation profiles within 30°N to 30°S obtained during 2006–2016 by VEx and Akatsuki reveals that this cycle implies night-time variations of 2–6% in atmospheric temperature, pressure and molecular density (see Figure S1).

The sharp cloud discontinuity is a recurrent phenomenon at both lower and middle clouds (Figures 1b and 2a; see Movie S2), although it is apparently missing in observations of the upper clouds (Satoh et al., 2017; Yamazaki et al., 2018) (Figure 2c). The discontinuity is sometimes followed by undulations with wavelengths of 65 ± 14 km (Figure 2b) and can also extend thousands of kilometers westward from their northernmost end giving birth to sharp dark stripes (Figures 1a and 1d) previously reported (Peralta et al., 2019). Table S1 in the supporting information contains a summary of all the events of cloud disruptions. During 2016, 35 events were identified in the Akatsuki observations (Figures S2 and S3), and probably two more in observations with small telescopes (Figures S4a and S4b). IRTF/SpeX observations between 2017 and 2019 revealed seven events (Figures S4c–S4d). A reanalysis of published ground-based observations (Allen & Crawford, 1984; Bailey, 2006; Crisp et al., 1991; Peralta et al., 2018) shows that the disruption was present on Venus's lower clouds in September 1983, January–February 1990, December 2005, July 2012 (Figure 2d), and at least 12 times during 2006–2008 in VEx/VIRTIS images (see Figures S4e–S4h).

VEx/VIRTIS images were used to study other effects of the disruption. On the nightside, the passage of the discontinuity implies radiance decreases of 75 ± 7%, 88 ± 7%, and 88 ± 6% at 1.74, 2.26, and 2.32 μm, respectively (see Table S2), while on dayside IR1/900-nm images it implies albedo changes of only 1–4% (Peralta et al., 2019). The optical thickness (Figure 3b) is observed to increase 1 order of magnitude west-to-east across the disruption, while its effect over the size parameter (regarded to be a proxy for particle size; see Carlson et al., 1993) is more variable although the westside of the disruption is frequently linked to more abundance of smaller particles (Figure 3c). This scenario seems consistent with downwelling and clouds' evaporation (McGouldrick et al., 2012) (hence, lower optical thickness) west of the disruption and upwelling accompanied by formation of clouds (larger optical thickness) on its eastside. This upwelling combined with the increased H_2SO_4 vapor pressure and the larger nucleation rates expected for the high H_2SO_4 concentrations of the clouds (Sihto et al., 2009; Titov et al., 2018) can help the cloud condensation nuclei (CNN) of submicron size to overcome the Kelvin barrier (i.e., greater saturation pressure over smaller particles) and grow to small droplets with radii of ~1 μm (Imamura & Hashimoto, 2001), probably explaining the abundance of smaller particles observed in Figure 3c.

Figure 3a displays the rotation period, orientation, and latitudinal extent of the disruption from 2016 until early 2019. The disruption appears within latitudes 30°N to 40°S, it can have a length that varies from 800 ± 50 to 7,600 ± 200 km and has a mean width of 280 ± 140 km (cross-to-along ratio ~1:13). Its mean orientation relative to the equatorial plane is 85° ± 18° but ranges from 35° to 132°. In rare cases, the cloud discontinuity is seen split into two or three elements with different orientations (Figure 2c). During August 2016, the disruption kept approximately coherent for ~20 days. However, in general, the disruption suffers distinguishable changes after one revolution (Figures 2a and S2), and its morphology and hemispherical symmetry/asymmetry seem unrelated to surface elevations (see Figure S5). The disruption propagates to the west with a mean zonal speed of −91 ± 9 m s^{-1}—similar to the equatorial jet when this is present (Horinouchi et al., 2017)—and faster than the background winds within 30°N to 40°S (see Figure 1e), which are −68 ± 9 m s^{-1} at the lower clouds (48–55 km) (Peralta et al., 2018) and −74 ± 9 m s^{-1} at the middle clouds (~55–65 km) (Peralta et al., 2019; Sánchez-Lavega et al., 2017). Considering the overall data, the rotation period of this disruption is 4.9 ± 0.5 days (Figure 3a). Separate analyses of data for the middle and lower

clouds yield periods of 4.7 ± 0.4 and 5.0 ± 0.5 days, respectively. The zonal drift of the disruption experienced larger variations in September (10 m s^{-1}) and November 2016 (~30 m s^{-1}). Observations during November 2018 and January 2019 suggest that the drift of this feature increased by 40 m s^{-1} during its propagation on the dayside (Figures 3a and 1e).

Considering its morphology, long-term coherence and its westward drift faster than the mean flow, the disruption might be the manifestation of a weakly dispersive Kelvin front (a nonlinear Kelvin wave). Kelvin fronts can be often undular like observed in Figure 2b, exhibiting gravity wave resonances excited behind the leading edge and propagating with the same phase speed (Fedorov & Melville, 2000). Day-night differences in stability and wind shear can change the intrinsic phase speed of a Kelvin wave (Peralta et al., 2015) and explain its faster propagation during its dayside passage (Figure 3a). Simulations of the deeper clouds with the IPSL Venus GCM (Garate-Lopez & Lebonnois, 2018) (which does not incorporate interactions between circulation and clouds' processes) show that Kelvin fronts arise between 45–68 km under realistic atmospheric conditions (Scarica et al., 2019), they affect zonal and meridional speeds and—more weakly—temperatures (Figure 4), and they barely interact with mountain waves (Figure S6). At 55 km, convection dominates vertical motions, explaining why the Kelvin wave is not apparent in Figure 4g. The sharpest gradient/discontinuity in zonal winds is found at 57 km (Figure 4b) and periodograms at different altitudes (Figure 4h) evidence that the wave is trapped within the deeper clouds with a westward rotation period of ~5.7 days, slower than the 4.9-day average from observations but between minimum/maximum periods reported. The rotation period is sensitive to the zonal winds below the clouds, being closer to observations when setting the relaxed profile of winds in the GCM (see section 2.4).

4. Conclusions

While stationary waves seem abundant at the upper clouds of Venus (56.5–70 km), the middle and lower clouds (47.5–56.5 km) do not exhibit stationary waves but a dark band with cyclical behavior and a sharp cloud discontinuity at equatorial latitudes with long-term coherence and apparently unrelated to the Venusian topography. The absence of observable signatures of this discontinuity at the upper clouds, where waves exhibit an evanescent nature (Imai et al., 2019) contrasts with its quasi-permanent nature at the middle and lower clouds.

Simulations with the IPSL Venus GCM show that a nonlinear Kelvin wave generated below the clouds (Yamamoto & Tanaka, 1997) reasonably reproduces this disruption and many of its observed properties (Figure 4). Bore waves generated by katabatic fronts at the surface (Sta. Maria Magdalena et al., 2006) or at higher altitudes by convective entrainment (Haghi et al., 2017) are alternative explanations to be explored by future studies, which might elucidate the role of this feature in the transport of atmospheric momentum and aerosols in the clouds of Venus.

Acknowledgments
The Akatsuki data set is available at JAXA's public repository (http://darts.isas.jaxa.jp/planet/project/akatsuki/). IRTF/SpeX images can be requested on reasonable request and will become available at the NASA/IPAC Infrared Science Archive (https://irsa.ipac.caltech.edu/applications/irtf/). VEx data set is available at ESA's public repository (ftp://psa.esac.esa.int/pub/mirror/VENUS-EXPRESS/). Data S1 includes the IPSL Venus GCM simulations of Figure 4 and they can be downloaded from Zenodo (https://zenodo.org/record/3817479). J. P. acknowledges JAXA's International Top Young Fellowship. T. N. and G. S. thank NASA's Grant NNX16AC84G. A. S. -L. and R. H. were supported by Spanish project AYA2015-65041-P (MINECO/FEDER, UE) and Grupos Gobierno Vasco IT-765-13. N. I. thanks partial support by JSPS KAKENHI Grant JP16H02225. Y. J. L. received funding from EU H2020 MSCA-IF 841432. P. M. acknowledges FCT's project P-TUGA PTDC/FIS-AST/29942/2017. S. S. L. thanks NASA's Grant NNX16AC79G. All authors acknowledge the hard work done by the Akatsuki team. Sincere thanks to James O'Donoghue for proofreading this paper.

References

Allen, D. A., & Crawford, J. W. (1984). Cloud structure on the dark side of Venus. *Nature*, *307*, 222–224.

Ando, H., Imamura, T., Tellmann, S., Pätzold, M., Häusler, B., Sugimoto, N., et al. (2020). Thermal structure of the Venusian atmosphere from the sub-cloud region to the mesosphere as observed by radio occultation. *Scientific Reports*, *10*, 3448. https://doi.org/10.1038/s41598-020-59278-8

Bailey, J. (2006). Probing the atmosphere of Venus using Infrared spectroscopy. In *Proceedings of the 6th australian space science conference*, Citeseer, pp. 23.

Carlson, R. W., Kamp, L. W., Baines, K. H., Pollack, J. B., Grinspoon, D. H., Encrenaz, Th., et al. (1993). Variations in Venus cloud particle properties: A new view of Venus's cloud morphology as observed by the Galileo near-infrared mapping spectrometer. *Planetary and Space Science*, *41*(7), 477–485. https://doi.org/10.1016/0032-0633(93)90030-6

Counselman, C. C., Gourevitch, S. A., King, R. W., Loriot, G. B., & Ginsberg, E. S. (1980). Zonal and meridional circulation of the lower atmosphere of Venus determined by radio interferometry. *Journal of Geophysical Research*, *85*, 8026–8030.

Crisp, D., McMuldroch, S., Stephens, S. K., Sinton, W. M., Ragent, B., Hodapp, K.-W., et al. (1991). Ground-based near-infrared imaging observations of Venus during the Galileo encounter. *Science*, *253*, 1538–1541.

Drossart, P., Piccioni, G., Adriani, A., Angrilli, F., Arnold, G., Baines, K. H., et al. (2007). Scientific goals for the observation of Venus by VIRTIS on ESA/Venus express mission. *Planetary and Space Science*, *55*, 1653–1672. https://doi.org/10.1016/j.pss.2007.01.003

Fedorov, A. V., & Melville, W. K. (2000). Kelvin fronts on the equatorial thermocline. *Journal of Physical Oceanography*, *30*(7), 1692. https://doi.org/10.1175/1520-0485(2000)030<1692:KFOTET>2.0.CO;2

Fukuhara, T., Futaguchi, M., Hashimoto, G. L., Horinouchi, T., Imamura, T., Iwagaimi, N., et al. (2017). Large stationary gravity wave in the atmosphere of Venus. *Nature Geoscience*, *10*, 85–88. https://doi.org/10.1038/ngeo2873

Garate-Lopez, I., & Lebonnois, S. (2018). Latitudinal variation of clouds' structure responsible for Venus' cold collar. *Icarus*, *314*, 1–11. https://doi.org/10.1016/j.icarus.2018.05.011

Haghi, K. R., Parsons, D. B., & Shapiro, A. (2017). Bores observed during IHOP_2002: The relationship of bores to the nocturnal environment. *Monthly Weather Review*, *145*(10), 3929–3946. https://doi.org/10.1175/MWR-D-16-0415.1

Hinson, D. P., & Jenkins, J. M. (1995). Magellan radio occultation measurements of atmospheric waves on Venus. *Icarus*, *114*, 310–327. https://doi.org/10.1006/icar.1995.1064

Horinouchi, T., Murakami, S., Satoh, T., Peralta, J., Ogohara, K., Kouyama, T., et al. (2017). Equatorial jet in the lower to middle cloud layer of Venus revealed by Akatsuki. *Nature Geoscience*, *10*, 646–651. https://doi.org/10.1038/ngeo3016

Imai, M., Kouyama, T., Takahashi, Y., Yamazaki, A., Watanabe, S., Yamada, M., et al. (2019). Planetary-scale variations in winds and UV brightness at the Venusian cloud top: Periodicity and temporal evolution. *Journal of Geophysical Research: Planets*, *124*, 2635–2659. https://doi.org/10.1029/2019JE006065

Imamura, T., & Hashimoto, G. L. (2001). Microphysics of Venusian clouds in rising tropical air. *Journal of Atmospheric Sciences*, *58*(23), 3597–3612. https://doi.org/10.1175/1520-0469(2001)058<3597:MOVCIR>2.0.CO;2

Imamura, T., Higuchi, T., Maejima, Y., Takagi, M., Sugimoto, N., Ikeda, K., & Ando, H. (2014). Inverse insolation dependence of Venus' cloud-level convection. *Icarus*, *228*, 181–188. https://doi.org/10.1016/j.icarus.2013.10.012

Iwagami, N., Sakanoi, T., Hashimoto, G. L., Sawai, K., Ohtsuki, S., Takagi, S., et al. (2018). Initial products of Akatsuki 1-μm camera. *Earth, Planets, and Space*, *70*, 6. https://doi.org/10.1186/s40623-017-0773-5

Kouyama, T., Taguchi, M., Fukuhara, T., Imamura, T., Horinouchi, T., Sato, T. M., et al. (2019). Global structure of thermal tides in the upper cloud layer of Venus revealed by LIR on board Akatsuki. *Geophysical Research Letters*, *46*, 9457–9465. https://doi.org/10.1029/2019GL083820

Lebonnois, S., Hourdin, F., Eymet, V., Crespin, A., Fournier, R., & Forget, F. (2010). Superrotation of Venus' atmosphere analyzed with a full general circulation model. *Journal of Geophysical Research*, *115*, E06006. https://doi.org/10.1029/2009JE003458

Lebonnois, S., Sugimoto, N., & Gilli, G. (2016). Wave analysis in the atmosphere of Venus below 100-km altitude, simulated by the LMD Venus GCM. *Icarus*, *278*, 38–51. https://doi.org/10.1016/j.icarus.2016.06.004

Lefèvre, M., Lebonnois, S., & Spiga, A. (2018). Three dimensional turbulence resolving modeling of the Venusian cloud layer and induced gravity waves: Inclusion of complete radiative transfer and wind shear. *Journal of Geophysical Research: Planets*, *123*, 2773–2789. https://doi.org/10.1029/2018JE005679

Limaye, S. S., Watanabe, S., Yamazaki, A., Yamada, M., Satoh, T., Sato, T. M., et al. (2018). Venus looks different at different wavelengths: Morphology from Akatsuki multispectral images. *Earth, Planets, and Space*, *70*, 38. https://doi.org/10.1186/s40623-018-0789-5

McGouldrick, K., Momary, T. W., Baines, K. H., & Grinspoon, D. H. (2012). Quantification of middle and lower cloud variability and mesoscale dynamics from Venus Express/VIRTIS observations at 1.74 μm. *Icarus*, *217*, 615–628. https://doi.org/10.1016/j.icarus.2011.07.009

Nakamura, M., Imamura, T., Ishii, N., Abe, T., Kawakatsu, Y., Hirose, C., et al. (2016). AKATSUKI returns to Venus. *Earth, Planets and Space*, *68*(1), 1–10. https://doi.org/10.1186/s40623-016-0457-6

Navarro, T., Schubert, G., & Lebonnois, S. (2018). Atmospheric mountain wave generation on Venus and its influence on the solid planet's rotation rate. *Nature Geoscience*, *11*(7), 487–491. https://doi.org/10.1038/s41561-018-0157-x

Ogohara, K., Takagi, M., Murakami, S.-Y., Horinouchi, T., Yamada, M., Kouyama, T., et al. (2017). Overview of Akatsuki data products: Definition of data levels, method and accuracy of geometric correction. *Earth, Planets, and Space*, *69*, 167. https://doi.org/10.1186/s40623-017-0749-5

Peralta, J., Hueso, R., Sánchez-Lavega, A., Lee, Y. J., Muñoz, A. G., Kouyama, T., et al. (2017). Stationary waves and slowly moving features in the night upper clouds of Venus. *Nature Astronomy*, *1*, 0187. https://doi.org/10.1038/s41550-017-0187

Peralta, J., Hueso, R., Sánchez-Lavega, A., Piccioni, G., Lanciano, O., & Drossart, P. (2008). Characterization of mesoscale gravity waves in the upper and lower clouds of Venus from VEX-VIRTIS images. *Journal of Geophysical Research*, *113*, E00B18. https://doi.org/10.1029/2008JE003185

Peralta, J., Iwagami, N., Sánchez-Lavega, A., Lee, Y. J., Hueso, R., Narita, M., et al. (2019). Morphology and dynamics of Venus's middle clouds with Akatsuki/IR1. *Geophysical Research Letters*, *46*, 2399–2407. https://doi.org/10.1029/2018GL081670

Peralta, J., Muto, K., Hueso, R., Horinouchi, T., Sánchez-Lavega, A., Murakami, S.-Y., et al. (2018). Nightside winds at the lower clouds of Venus with Akatsuki/IR2: Longitudinal, local time and decadal variations from comparison with previous measurements. *The Astrophysical Journal Supplement Series*, *239*(29), 17. https://doi.org/10.3847/1538-4365/aae844/meta

Peralta, J., Sánchez-Lavega, A., Horinouchi, T., McGouldrick, K., Garate-Lopez, I., Young, E. F., et al. (2019). New cloud morphologies discovered on the Venus's night during Akatsuki. *Icarus*, *333*, 177–182. https://doi.org/10.1016/j.icarus.2019.05.026

Peralta, J., Sánchez-Lavega, A., López-Valverde, M. A., Luz, D., & Machado, P. (2015). Venus's major cloud feature as an equatorially trapped wave distorted by the wind. *Geophysical Research Letters*, *42*, 705–711. https://doi.org/10.1002/2014GL062280.

Rayner, J., Bond, T., Bonnet, M., Jaffe, D., Muller, G., & Tokunaga, A. (2012). iSHELL: A 1-5 micron cross-dispersed R=70,000 immersion grating spectrograph for IRTF. In I. S. McLean, S. K. Ramsay, & H. Takami (Eds.), *Ground-based and airborne instrumentation for astronomy iv* (Vol. 8446, pp. 832–843). Amsterdam, Netherlands: SPIE. https://doi.org/10.1117/12.925511

Rayner, J. T., Toomey, D. W., Onaka, P. M., Denault, A. J., Stahlberger, W. E., Vacca, W. D., et al. (2003). SpeX: A medium-resolution 0.8-5.5 micron spectrograph and imager for the NASA infrared telescope facility. *The Publications of the Astronomical Society of the Pacific*, *115*, 362–382. https://doi.org/10.1086/367745

Sánchez-Lavega, A., Lebonnois, S., Imamura, T., Read, P., & Luz, D. (2017). The atmospheric dynamics of Venus. *Space Science Reviews*, *212*, 1541–1616. https://doi.org/10.1007/s11214-017-0389-x

Sánchez-Lavega, A., Peralta, J., Gomez-Forrellad, J. M., Hueso, R., Pérez-Hoyos, S., Mendikoa, I., et al. (2016). Venus cloud morphology and motions from ground-based images at the time of the Akatsuki orbit insertion. *The Astrophysical Journal Letters*, *833*, L7. https://doi.org/10.3847/2041-8205/833/1/L7

Satoh, T., Sato, T. M., Nakamura, M., Kasaba, Y., Ueno, M., Suzuki, M., et al. (2017). Performance of Akatsuki/IR2 in Venus orbit: The first year. *Earth, Planets, and Space*, *69*, 154. https://doi.org/10.1186/s40623-017-0736-x

Scarica, P., Garate-Lopez, I., Lebonnois, S., Piccioni, G., Grassi, D., Migliorini, A., & Tellmann, S. (2019). Validation of the IPSL Venus GCM thermal structure with Venus Express data. *Atmosphere*, *10*(10), 584. https://doi.org/10.3390/atmos10100584

Sihto, S. L., Vuollekoski, H., Leppä, J., Riipinen, I., Kerminen, V. M., Korhonen, H., et al. (2009). Aerosol dynamics simulations on the connection of sulphuric acid and new particle formation. *Atmospheric Chemistry & Physics*, *9*(9), 2933–2947.

Sta. Maria Magdalena, R. V., Scot, C. R. R., & Timothy, I. M. (2006). Numerical simulation of atmospheric bore waves on Mars. *Icarus*, *185*(2), 383–394. https://doi.org/10.1016/j.icarus.2006.07.006

Tellmann, S., Pätzold, M., Häusler, B., Bird, M. K., & Tyler, G. L. (2009). Structure of the Venus neutral atmosphere as observed by the Radio Science experiment VeRa on Venus Express. *Journal of Geophysical Research*, *114*, E00B36. https://doi.org/10.1029/2008JE003204

Titov, D. V., Ignatiev, N. I., McGouldrick, K., Wilquet, V., & Wilson, C. F. (2018). Clouds and hazes of Venus. *Space Science Reviews*, *214*(8), 126. https://doi.org/10.1007/s11214-018-0552-z

Wilson, C. F., Guerlet, S., Irwin, P. G. J., Tsang, C. C. C., Taylor, F. W., Carlson, R. W., et al. (2008). Evidence for anomalous cloud particles at the poles of Venus. *Journal of Geophysical Research*, *113*, E00B13. https://doi.org/10.1029/2008JE003108

Yakovlev, O. I., Matyugov, S. S., & Gubenko, V. N. (1991). Venera-15 and -16 middle atmosphere profiles from radio occultations: Polar and near-polar atmosphere of Venus. *Icarus*, *94*(2), 493–510. https://doi.org/10.1016/0019-1035(91)90243-M

Yamamoto, M., & Tanaka, H. (1997). Formation and maintenance of the 4-day circulation in the Venus middle atmosphere. *Journal of Atmospheric Sciences*, *54*, 1472–1489. https://doi.org/10.1175/1520-0469(1997)054<1472:FAMOTD>2.0.CO;2

Yamazaki, A., Yamada, M., Lee, Y. J., Watanabe, S., Horinouchi, T., Murakami, S., et al. (2018). Ultraviolet imager on Venus orbiter Akatsuki and its initial results. *Earth, Planets and Space*, *70*(1), 23. https://doi.org/10.1186/s40623-017-0772-6